AGU PUBLICATIONS

Geophysical Research Letters

RESEARCH LETTER
10.1002/2016GL070883

The shallow elastic structure of the lunar crust: New insights from seismic wavefield gradient analysis

David Sollberger[1], **Cedric Schmelzbach**[1], **Johan O. A. Robertsson**[1], **Stewart A. Greenhalgh**[2], **Yosio Nakamura**[3], **and Amir Khan**[1]

[1]Institute of Geophysics, ETH Zurich, Zurich, Switzerland, [2]Department of Earth Sciences, King Fahd University of Petroleum and Minerals, Dhahran, Saudi Arabia, [3]Institute for Geophysics, University of Texas at Austin, Austin, Texas, USA

Key Points:

- Spatial seismic wavefield gradients used to compute rotational motion and identify shear waves on complex single-component Apollo 17 data
- First comprehensive elastic-parameter model of the shallow lunar crust
- Rotational data analysis shown to significantly augment the information content of sparse seismic acquisition such as in planetary seismology

Supporting Information:

- Supporting Information S1

Correspondence to:
D. Sollberger,
david.sollberger@erdw.ethz.ch

Citation:
Sollberger, D., C. Schmelzbach, J. O. A. Robertsson, S. A. Greenhalgh, Y. Nakamura, and A. Khan (2016), The shallow elastic structure of the lunar crust: New insights from seismic wavefield gradient analysis, *Geophys. Res. Lett.*, *43*, doi:10.1002/2016GL070883.

Received 18 AUG 2016
Accepted 16 SEP 2016
Accepted article online 20 SEP 2016

Abstract Enigmatic lunar seismograms recorded during the Apollo 17 mission in 1972 have so far precluded the identification of shear-wave arrivals and hence the construction of a comprehensive elastic model of the shallow lunar subsurface. Here, for the first time, we extract shear-wave information from the Apollo active seismic data using a novel waveform analysis technique based on spatial seismic wavefield gradients. The star-like recording geometry of the active seismic experiment lends itself surprisingly well to compute spatial wavefield gradients and rotational ground motion as a function of time. These observables, which are new to seismic exploration in general, allowed us to identify shear waves in the complex lunar seismograms, and to derive a new model of seismic compressional and shear-wave velocities in the shallow lunar crust, critical to understand its lithology and constitution, and its impact on other geophysical investigations of the Moon's deep interior.

1. Introduction

The shallow lunar crust is presumed to consist of highly fractured basaltic material characterized by low seismic wave speed and very low intrinsic attenuation [*Latham et al.*, 1970; *Cooper et al.*, 1974]. These properties are thought to be responsible for intense scattering of seismic waves within the near-surface zone and to lead to the characteristic, long-duration reverberations following the first-arriving *P* wave observed on the seismograms recorded during the Apollo missions [*Gangi*, 1972]. The reverberations effectively obscure later-arriving shear waves, mode conversions, and reflections and have, so far, precluded the identification of these arrivals (Figure 1c). In addition, the propagation paths of waves traveling through the near-surface zone are short, causing refracted and reflected arrivals of different wave modes to be only poorly separated on the recordings, which further exacerbates the identification of such arrivals. As a consequence of the difficulty to interpret the lunar seismograms, the shear-wave velocity structure of the uppermost layers of the lunar subsurface is effectively unknown. This is a serious shortcoming because due to their complexity, the shallowest layers can have a significant impact on travel times and waveforms, not only for the upper crust but also for seismic arrivals from the deep interior of the Moon [*Weber et al.*, 2011]. Determination of the seismic velocities of the near-surface zone is therefore important and necessary to better characterize the shallow as well as the deep interior structure and elastic properties of the Moon [*Nakamura*, 1983; *Khan et al.*, 2000; *Lognonné et al.*, 2003; *Wieczorek et al.*, 2006].

The active seismic experiments that were carried out during the Apollo missions sought to explore the shallow lunar subsurface below the different landing sites [*Cooper et al.*, 1974]. During three missions (Apollo 14, 16, and 17), the astronauts deployed thumper sources, a mortar, and explosive packages (EPs) on the lunar surface to generate seismic signals. In these experiments, the vertical component of ground motion (particle velocity) was recorded on arrays of up to four geophones.

In this study, we applied a novel seismic data processing technique based on analysis of the horizontal spatial derivatives of the wavefield [e.g. *Schmelzbach et al.*, 2016] to the lunar seismic profiling experiment (LSPE) data from the Apollo 17 mission. The star-like geophone configuration of the Apollo 17 LSPE (Figures 1a and 1b) is more suitable for a spatial seismic wavefield gradient analysis than the linear array configurations employed during the Apollo 14 and 16 missions. A particular strength of spatial wavefield gradient

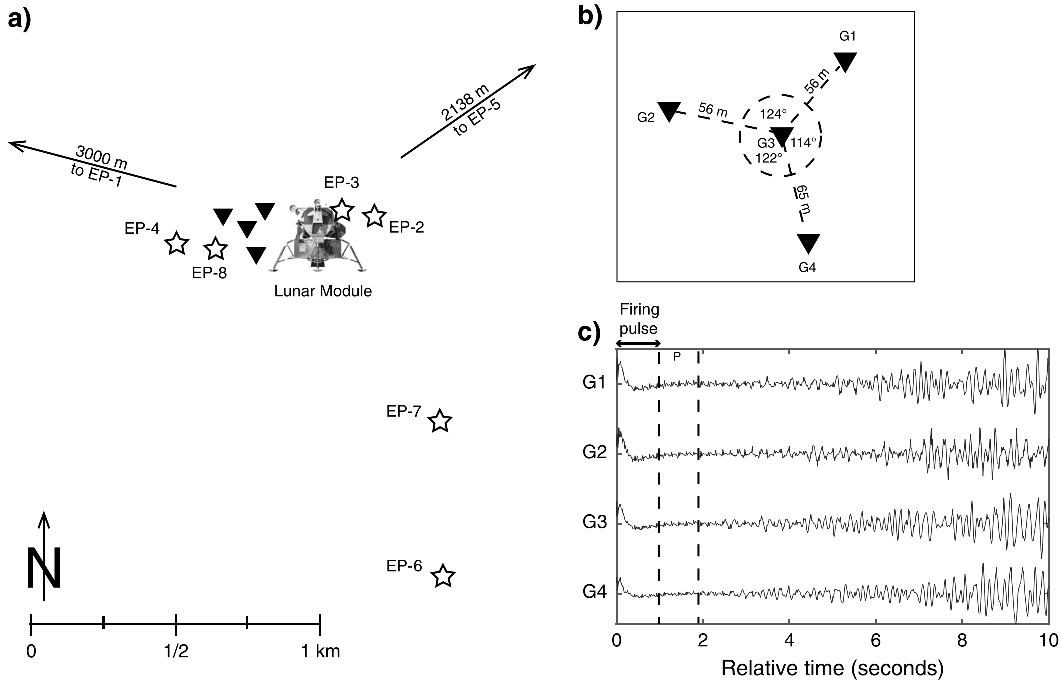

Figure 1. The Apollo 17 lunar seismic profiling experiment (LSPE). (a) Map of LSPE showing the locations of the four geophones (black triangles), the eight explosive packages (stars), and the lunar module (pictogram). (b) Detailed view of the geophone configuration. (c) Data recorded at the four geophones as a response to firing of EP-7. The firing pulse is represented on the data as cross talk (inductive pickup). The first-arriving *P* wave is at 1.9 s [after *Cooper et al.*, 1974]. Note the long trail of reverberations with increasing amplitudes following the first arrival.

analysis is that it enables the extraction of critical information, such as *S* wave travel times, from the very limited amount of conventional seismic data available from the LSPE. Our elastic-property model, derived from our new *S* wave picks, is based on the analysis of data from only seven seismic sources—six EPs and the surface impact from the ascent stage of the lunar module (LM)—recorded by a total number of four geophones.

2. Wavefield Gradient Analysis

Spatial gradients of the seismic wavefield can be calculated by a finite-difference approximation using the seismic records from a closely spaced geophone array. At the free surface, the spatial gradients of vertical-component recordings directly correspond to rotational ground motion [*Cochard et al.*, 2006; *Muyzert et al.*, 2012]. Measuring the spatial gradients at the free surface hence isolates *S* waves, since *P* waves do not have a rotational component [*Aki and Richards*, 2002]. Additionally, seismic gradient data yield estimates of wavefield parameters such as phase velocity, relative change in geometrical spreading, wave directionality, and radiation pattern [*Langston et al.*, 2006; *Langston*, 2007a; 2007b] and allow, for example, for local wavefield separation [*Robertsson and Curtis*, 2002; *Van Renterghem et al.*, 2016]. Unlike conventional techniques for determining such parameters (e.g., beam-forming using extended dense arrays), the gradient analysis can be applied to spatially compact arrays. *Curtis and Robertsson* [2002] used seismic gradients to extract near-surface *P* and *S* wave velocities. Recently, *de Ridder and Biondi* [2015] showed that wavefield gradient analysis also yields reasonable results for a stochastic wavefield of Scholte waves present in the ambient seismic noise field. Here we use the information contained in the spatial wavefield gradients to identify *S* waves and extract their travel times from the Apollo seismic data.

2.1. Measuring Wavefield Gradients

Consider a propagating wavefield that is sampled at $N+1$ spatial points by a surface array of closely spaced geophones. If the stations forming the array are spaced at a subwavelength interval, then we can solve the following set of linear equations, based on the first-order Taylor series expansion of the recorded three-component particle velocity field $\mathbf{v} = [v_x, v_y, v_z]^T$, to find the horizontal spatial gradients $\partial_x \mathbf{v}$ and $\partial_y \mathbf{v}$ of the wavefield [*Spudich et al.*, 1995; *Liang and Langston*, 2009]:

$$\begin{pmatrix} \mathbf{v}^1 - \mathbf{v}^0 \\ \mathbf{v}^2 - \mathbf{v}^0 \\ \vdots \\ \mathbf{v}^N - \mathbf{v}^0 \end{pmatrix} = \begin{pmatrix} x^1 - x^0 & y^1 - y^0 \\ x^2 - x^0 & y^2 - y^0 \\ \vdots & \vdots \\ x^N - x^0 & y^N - y^0 \end{pmatrix} \begin{pmatrix} \partial_x \mathbf{v} \\ \partial_y \mathbf{v} \end{pmatrix}. \tag{1}$$

Here $\mathbf{v}^i$ is particle velocity recorded at the ith station, $\mathbf{v}^0$ is the particle velocity at a reference station where the gradients are to be estimated, and x^i and y^i are the x and y coordinates of station i. Note that local perturbations, such as due to varying geophone-ground coupling conditions, lateral variations in wave speed, and inaccurate knowledge of the coordinates can lead to an erroneous estimate of the spatial gradients [*Poppeliers and Evans*, 2015; *Schmelzbach et al.*, 2016].

2.2. Rotational Ground Motion at the Free Surface

A seismic wavefield does not only exhibit translational but also rotational ground motion [*Aki and Richards*, 2002]. By measuring rotational ground motions, shear waves are effectively isolated, since compressional waves (*P* waves) are curl free [*Sollberger et al.*, 2016]. Rotation rates around the three Cartesian coordinate axes are given by the curl of the particle velocity wavefield:

$$\mathbf{r} = \frac{1}{2}\nabla \times \mathbf{v} = \frac{1}{2}\begin{pmatrix} \partial_y v_z - \partial_z v_y \\ \partial_z v_x - \partial_x v_z \\ \partial_x v_y - \partial_y v_x \end{pmatrix}. \tag{2}$$

Here $\mathbf{r} = [r_x, r_y, r_z]^T$ is the three-component rotation rate vector, and $\nabla = [\partial_x, \partial_y, \partial_z]^T$ is the vector differential operator composed of the partial derivatives with respect to the spatial coordinates x, y, and z. Equation (2) shows how rotational ground motion can be derived from spatial gradient measurements. Estimating the vertical derivatives ∂_z in equation (2) by a finite-difference approximation would require receivers buried at depth. However, at the free surface, the traction normal to the surface vanishes, which imposes additional constraints on the vertical derivatives ∂_z of the particle velocity [*Spudich et al.*, 1995; *Robertsson and Curtis*, 2002]:

$$\partial_z v_x = -\partial_x v_z, \tag{3}$$

$$\partial_z v_y = -\partial_y v_z. \tag{4}$$

Substituting equations (3) and (4) into equation (2) yields the following expressions of the two horizontal components of rotational ground motion at the free surface:

$$r_x = \partial_y v_z, \tag{5}$$

$$r_y = -\partial_x v_z. \tag{6}$$

We thus find that the rotational ground motion around the two horizontal (x, y) axes corresponds to the horizontal spatial gradients of the vertical component of the particle velocity field, if the measurements are taken directly or immediately below the free surface. Equations (5) and (6) suggest a simple way to isolate the *S* wave component of the wavefield by measuring the spatial gradients. Note that incoming *P* waves at the free surface will also produce a small amount of rotational motion due to partial conversion of energy into reflected downgoing *S* waves. The amount of *S* wave energy created by an incoming *P* wave at the free surface depends on the inclination angle of the arrival and is zero for vertically incident *P* waves.

2.3. Apparent Phase Velocity and Propagation Direction Estimation

In addition to rotational ground motion, other wavefield parameters, such as the apparent phase velocity and the propagation direction, can be estimated by gradient analysis. For an isolated plane wave arrival crossing the array with apparent horizontal slowness components $p_x = \partial t/\partial x$ and $p_y = \partial t/\partial y$ (reciprocal of apparent horizontal velocity), the following relation holds, linking the spatial gradients $\partial_x v_z$ and $\partial_y v_z$ to the ground acceleration $\partial_t v_z$:

$$\partial_x v_z = -p_x \partial_t v_z, \text{ and } \partial_y v_z = -p_y \partial_t v_z. \tag{7}$$

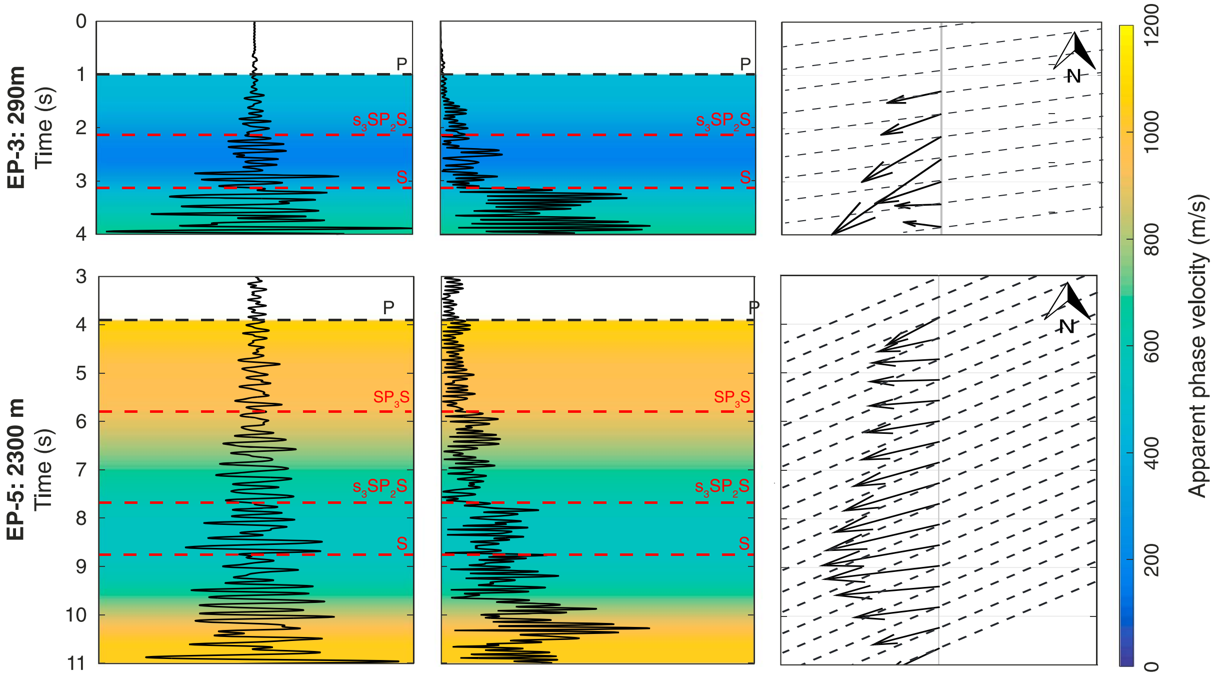

Figure 2. Gradient-based estimates of apparent phase velocity (color), rotational ground motion, and propagation direction for EP-3 and EP-5. Shear wave arrivals, identified based on their distinct increase in the amount of rotational energy, are marked in red. Dashed lines underlying the propagation direction estimates mark the source-receiver azimuth according to the survey geometry.

Thus, if the horizontal spatial gradients of the wavefield are known, estimates of the apparent horizontal slowness can be obtained from equation (7). The propagation azimuth ϕ is then obtained by $\tan\phi = p_y/p_x$. Equation (7) can be solved at each sample in time, yielding sample-by-sample estimates of p_x, p_y, and ϕ. In practice, interference of different arrivals in the coda of the seismogram will cause the estimated slowness to differ from the desired solution that would be obtained for an isolated arrival. Additionally, stabilization is needed to solve equation (7), because both the acceleration and the spatial gradient time series are highly oscillatory and cause singularities in the estimated slowness where zero crossings occur. To overcome this stability problem, equation (7) is usually solved either in the frequency domain [*Langston*, 2007a] or by the use of the analytic signal in the time domain [*Langston*, 2007c]. For the analysis of the lunar data, we applied the second approach.

3. Application to Apollo 17 Data

To mitigate aliasing of the spatial gradients (see supporting information Text S2), we filtered the LSPE data into low-frequency bands: 3 to 10 Hz for the computation of rotational motions and 3 to 3.5 Hz for the calculation of apparent phase velocities. The narrow-frequency band for the latter was chosen to avoid possible dispersion effects. We extracted the spatial wavefield derivatives from the filtered seismograms (equation (1)), computed the two horizontal components of rotational motion (equations (5) and 6), and applied the analytic signal approach to estimate apparent phase velocities (equation (7)) [*Langston*, 2007c]. We analyzed seismic signals generated by six EP's and the impact of the LM ascent stage on the lunar surface, 8.7 km southwest of the array. Our methodology could not be applied to the data from the two near-offset explosive packages EP-4 and EP-8, since the short apparent wavelengths of the waves associated with these events caused the spatial gradient estimates to be aliased (Text S2 and Figure S3).

As an example, the spatial gradient analysis results are shown for EP-3 and EP-5 in Figure 2 and show consistent rotational energy, apparent phase velocities, and propagation direction estimates across multiple seismic sources (Figure S1). As expected, the first-arriving *P* wave is associated with only minor rotational energy (sum of squares of the two components of rotational ground motion around orthogonal horizontal axes obtained by the spatial gradients). Generally, high apparent phase velocities are observed for the first-arriving *P* wave and decreasing phase velocities for later arrivals. The apparent phase velocity of the first-arriving *P* waves

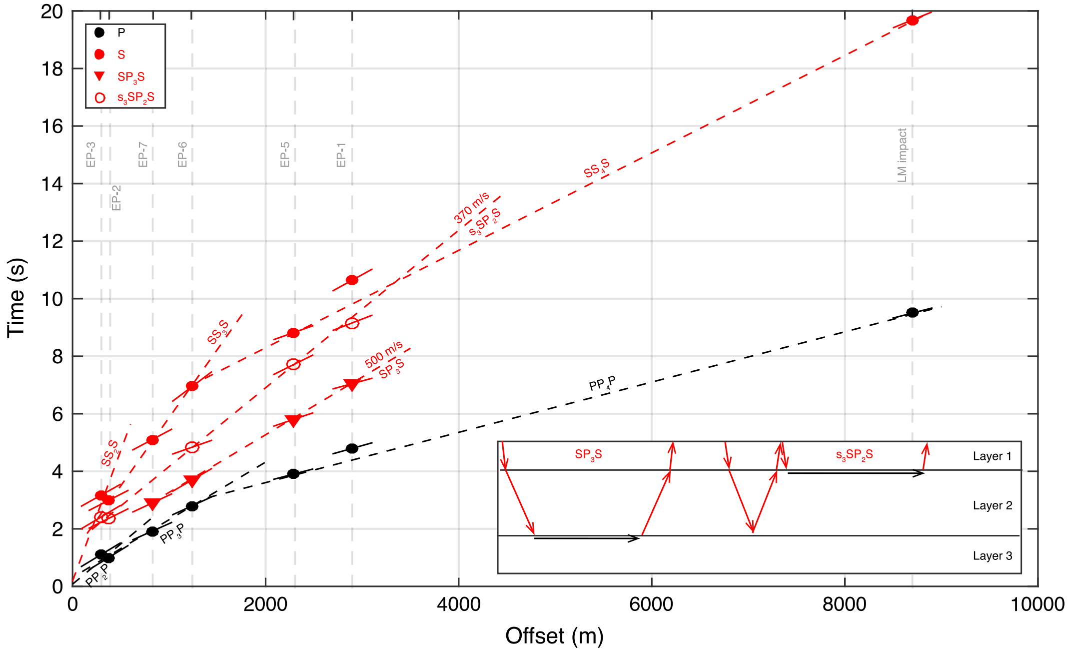

Figure 3. Extracted travel time curves for *P* and *S* waves. Travel time curves for *P* wave first arrivals, consistent with *Cooper et al.* [1974] in black, and *S* wave arrivals (in red) picked on the basis of gradient analysis. Travel times of the LM impact data are corrected for a reported clock error [*Nakamura*, 2011]. The slope of the short solid lines going through each pick corresponds to the apparent phase velocity that was estimated by spatial gradient analysis. Dashed lines indicate predicted travel times for different refracted modes using standard modeling of critically refracted arrivals in a layered medium and our preferred velocity model of the lunar near-surface structure (Figure 4). Subscripts in labeled arrivals denote the layer at which the wave is critically refracted or reflected, the first case letter (P or S) denotes the wave type of the downgoing wave, the second case letter denotes the wave mode of the critically refracted wave, and the third case letter denotes the wave type of the upgoing wave. Lower case letters correspond to the reflected wave type. Possible raypaths are shown as schematic drawings for the two shear wave arrivals showing apparent velocities of 500 m/s and 370 m/s (black arrows correspond to segments of the ray traveled as a *P* wave, red arrows to segments traveled as an *S* wave).

increases with increasing offset, indicating diving waves or critically refracted head waves from greater depths. Estimated propagation directions of the first-arriving *P* wave are consistent with the source-receiver azimuth from the survey geometry (marked by the dashed lines in Figure 2), which confirms the stability of the spatial gradient computation for these high-speed arrivals. Note that at late times, the estimated propagation direction deviates erratically from the expected direction. This could be caused by effects like interference of different wave modes or aliasing of the spatial gradient estimates of the low-speed waves arriving at late times.

3.1. Shear Wave Identification

We identified *S* waves based on the distinct higher amount of rotational motion relative to the first-arriving *P* wave (Figures 2 and S1 and Table S1). Since aliasing of the spatial gradient estimates and interference of different wave modes are likely to cause inaccuracies in the estimated phase velocities for late arrivals, a direct interpretation of the absolute values of these velocities should be done with caution. We used the gradiometry-based phase velocity and propagation direction estimates as an aid to evaluate the stability of the gradient computation. To avoid *S* wave travel time mispicks due to unstable gradient computation, we excluded time windows from the analysis for which the estimated propagation direction significantly deviates (> 45°) from the source-receiver azimuth or the phase velocity was likely heavily overestimated.

4. Seismic Velocity Structure of the Shallow Lunar Crust

The arrival times of the identified *S* waves naturally map onto straight line segments when plotted against offset (Figure 3), implying that these arrivals are critically refracted waves (head waves) from planar interfaces. Similar diagrams for picked first-arriving *P* waves were identified by *Cooper et al.* [1974]. Two distinct *S* wave

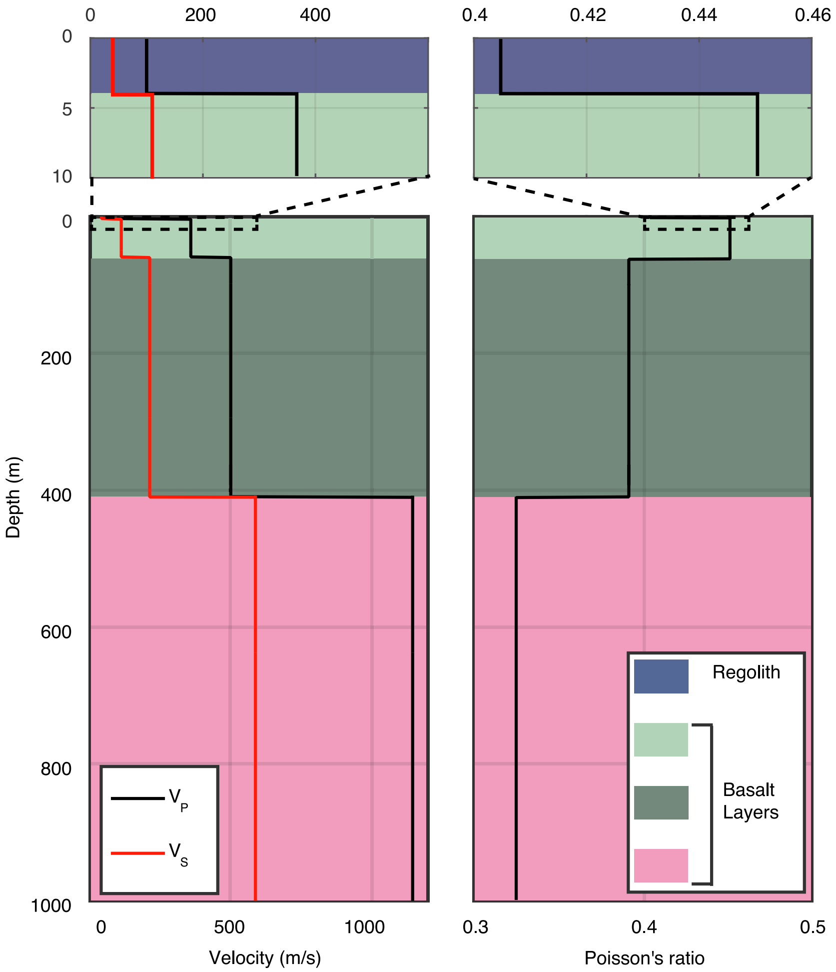

Figure 4. Recovered large-scale seismic velocity and Poisson's ratio structure of the lunar crust below the Apollo 17 landing site. Note that synthetic data tests revealed that small-scale velocity variations are very pronounced in each layer (Figure 5). These variations are estimated to be 70% in the first and second layer, 50% in the third layer, and 25% in the half-space below.

arrivals display linear move-out with velocities of 370 m/s and 500 m/s, which are very similar to the *P* wave velocities of the two shallowest refractors in the reference model of *Cooper et al.* [1974] (327 m/s and 495 m/s). This similarity in velocity suggests that the arrivals correspond to mode-converted refracted waves that travel just below the refractor interface at the *P* wave velocity but arrive at the geophone array as *S* waves (inset in Figure 3). Such mode-converted arrivals can be used to better constrain the velocities and depths of the corresponding refractors.

Assuming a horizontally layered medium, we searched for a velocity model that minimizes the difference between the identified (observed) *P* and *S* wave travel times and the predicted travel times obtained from standard seismic refraction modeling for both pure-mode and mode-converted refracted arrivals. Using a classic travel time-offset curve analysis [e.g., *Telford et al.*, 1990], we arrived at a three-layer model overlying a half-space (Figure 4) with *P* wave velocities of 100 m/s, 370 m/s, 500 m/s, and 1100 m/s and corresponding *S* wave velocities of 40 m/s, 110 m/s, 210 m/s, and 580 m/s, respectively. The layer depths are 4 m, 60 m, and 410 m, respectively. Due to the lack of near-offset information, the depth and seismic velocities of the first layer could not be resolved by our analysis and are therefore adapted from previous publications by *Cooper et al.* [1974] for the *P* waves and *Larose et al.* [2005] for the *S* waves.

Considering the mode-converted arrivals, the *S* wave arrival having an apparent velocity of 500 m/s (SP_3S in Figure 3) can be explained as a wave that travels from the source down to the top of the third layer as an *S* wave, where it is critically refracted as a *P* wave and then returns to the surface as a mode-converted *S* wave. The late intercept time of the S wave having a low apparent velocity of 370 m/s can be explained by a more complex travel path involving reflection at the third layer and at the free surface (s_3SP_2S in Figure 3). Note that the arrivals of EP-2 arrive slightly earlier than the arrivals of EP-3 despite the larger offset, which can be attributed to interface topography at the top of the third layer [*Cooper et al.*, 1974]. Also, the pure-mode first-arriving P wave from EP-1 is assumed to be delayed by 0.3 s when passing through the crater Camelot that lies on its travel path [*Kovach and Watkins*, 1973]. We found the Camelot-related delay to be 0.77 s for the S wave.

A comparison of the phase velocities obtained by seismic gradient analysis and the velocities in our best-fitting model shows that reasonable phase velocity estimates are obtained for the fast and isolated P waves. The mismatch is largest for near-offset arrivals in the coda, where aliasing due to low apparent phase velocities (Text S2) and interference are likely to occur. Note that the velocities of the deepest layer in the model are only poorly constrained from the travel time curve, due to the lack of data at far offsets. Additionally, because of a clock error, uncertainties remain about the actual zero time of the LM impact data [*Nakamura*, 2011], from which the velocity of the deepest layer is obtained. However, the phase velocities obtained by spatial gradient analysis provide source-time independent information on the velocities of this layer. We expect that the errors in the estimated phase velocities are smallest for the far-offset events (Figure S8), where the different waves are better separated in time and aliasing is reduced due to the high apparent velocities of the arrivals. Indeed, the estimated phase velocity of the first-arriving P wave of the LM impact event (1074 m/s) is very similar to that of EP-5 (1140 m/s), confirming recent findings that the 1000 m/s layer found by *Cooper et al.* [1974] extends to greater depth than previously thought [*Nakamura*, 2011].

Our analysis suggests that the shallow lunar crust at the Apollo 17 landing site consists of distinct layers that differ in composition (i.e., basalt layers) and/or physical state (e.g., porosity). Based on the P and S wave speeds in each layer, we find a high Poisson's ratio close to the surface (> 0.4) and generally decreasing Poisson's ratio with depth. Our results are consistent with findings in previous studies where seismic velocities were obtained by the analysis of horizontal-to-vertical seismic component spectral ratios at other landing sites [*Horvath et al.*, 1980] and by laboratory experiments on lunar soil samples, yielding Poisson's ratios of about 0.40 for the shallowest layers [*Stesky and Renton*, 1977]. Our recovered elastic-parameter model supports the current understanding of the lunar near-surface structure that a thin layer of low-velocity lunar regolith overlies distinct layers of heavily fractured, porous basaltic material [*Talwani et al.*, 1974]. The overall decrease of the Poisson's ratio with depth likely indicates a decrease in porosity (fracture density) with depth, which is consistent with recent results from the Gravity Recovery and Interior Laboratory (GRAIL) mission [*Besserer et al.*, 2014].

5. Synthetic Data Verification

We conducted a synthetic data study in order to verify the arrival times of the identified waves in Figure 3 and the velocity model in Figure 4. Synthetic data were generated using a time-domain finite-difference modeling method for heterogeneous elastic media [*Virieux*, 1986]. Since the source signatures of the Apollo 17 seismic sources are unknown, we used a Ricker wavelet with a center frequency of 3 Hz as a source wavelet. Rotational seismograms were derived from the modeled translational seismograms at neighboring grid points by using a finite-difference approximation. All simulations were performed in 2-D for computational efficiency.

Figure 5b shows the synthetic seismograms obtained using our preferred velocity model, which consists of four discrete constant-velocity layers (Figure 4). For this model, the travel times of the direct and refracted S waves match very well with the picked travel times, and also the distinct observed changes in rotational energy can well be reproduced from the synthetic data. Yet the amount of energy arriving before the direct shear wave is much lower in the synthetic data than in the real data (Figure 5a) for both the translational and the rotational components. We attribute the rotational energy present in the real data but missing in the synthetic data, to scattering due to small-scale variations, which were not included in the constant-velocity layer model. To simulate scattering in the highly heterogeneous lunar crust, we introduced stochastic velocity fluctuations using a von Kármán model [*Goff and Holliger*, 2003; *Korn*, 1993] and recomputed the synthetic seismograms. We explored a model space by allowing the velocity fluctuations in each layer in Figure 4 to vary up to a maximum of 75%. Figure 5c shows the synthetic seismograms that visually agreed best with the real data. A good fit between real and synthetic data was found for a model where the heterogeneity decreases with depth. Velocity variations are 70% in the first (lunar regolith) and the second layer, 50% in the third layer, and 25% in the half-space below. The amplitude characteristics of both the translational and rotational

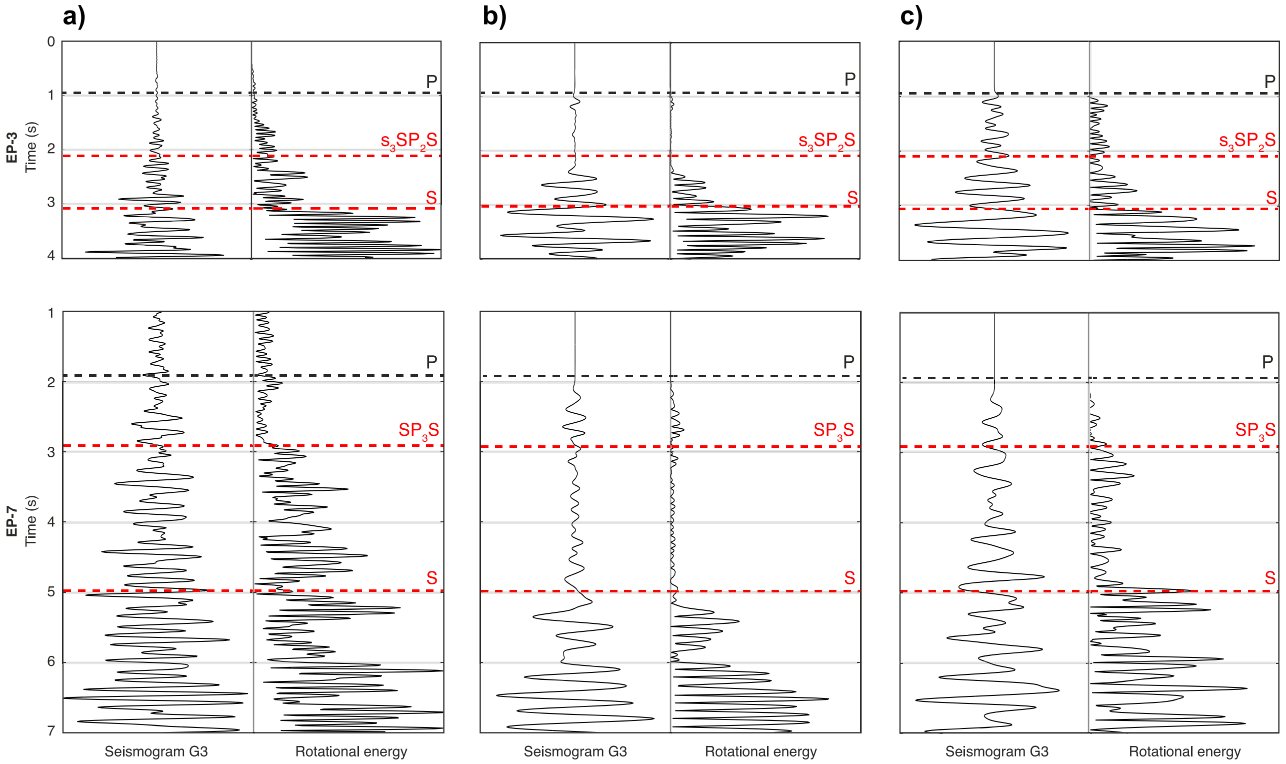

Figure 5. Comparison of real and synthetic data for EP-3 and EP-7. (a) Real data seismograms and rotational energy shown for EP-3 and EP-7. (b) Synthetic data obtained by finite-difference modeling using our preferred velocity model (Figure 4) of four homogeneous layers without scattering. Note the distinct higher amount of rotational ground motion associated with the shear wave arrival. (c) Synthetic data obtained using the same model but with stochastic fluctuations added to simulate scattering. The amount of rotational energy arriving before the direct shear wave (*S*) is increased compared to the simulations without stochastic fluctuation. This is in better agreement with the real data. Note that the refracted and mode-converted arrivals can still be identified based on their higher amount of rotational energy.

seismograms are in better agreement with the real data, when compared to the model without scattering. Despite the high amount of scattering, the refracted and mode-converted *S* wave arrivals can still be identified based on the step-like increase in rotational energy associated with their arrival at the expected times (Figures S4–S7), which implies that the impact of the layer structure on the wave propagation dominates over the stochastic fluctuations. These results indicate that rotational energy is indeed a useful diagnostic to identify *S* wave arrivals in complex reverberatory seismic data. Our synthetic tests confirm that the heterogeneity in the shallow lunar crust is extremely pronounced, most likely due to continuous meteorite impacts leading to a decrease of porosity with depth.

6. Conclusions

Our successful spatial seismic wavefield gradient analysis study of the Apollo 17 data, yielding the first elastic model of the shallow lunar crust, demonstrates that the analysis of wavefield gradients and rotational data has a great potential for future space missions that aim to explore the interior structure of extraterrestrial objects by seismic methods. A large amount of critical information can be extracted from spatially compact geophone arrays with a small number of stations and using only a limited number of sources. Future scientific experiments could likely be optimized by employing a more favorable geophone configuration, especially designed for the purposes of spatial gradient analysis. A seismic wavefield gradient experiment can either consist of an array of closely spaced three-component geophones or of a single six-component sensor measuring both translational and rotational motions simultaneously. A well-calibrated seismic gradient experiment can effectively enable the continuous estimation of apparent phase velocity, propagation direction, and wave type of seismic arrivals without the need to know the event location and origin time. This information, which is conventionally only obtained from dense, large-aperture arrays, greatly enhances the interpretation of the recorded seismograms.

We expect that the proposed methodology of identifying shear waves on vertical component seismic data can also be applied to the routinely recorded data from land seismic exploration on Earth. In particular, we anticipate that seismic wavefield gradient data will help to better characterize the complex near-surface zone. Additionally, we see a great potential of our method, as well as of wavefield gradient and rotational data analyses in general, for seismic exploration with sparse small arrays and/or at sites with limited access, such as boreholes, the ocean bottom, or mine and tunneling environments.

Acknowledgments
This study was supported by the CARNEVAL industry consortium (Nagra, OMV, Schlumberger Gould Research). The original seismic data of the Apollo missions are archived at the NSSDC (http://nssdc.gsfc.nasa.gov/) and were converted to SEG-Y format by *Brzostowski and Brzostowski* [2009]. We thank three anonymous reviewers for their comments, which helped us to greatly improve the manuscript.

References

Aki, K., and P. G. Richards (2002), *Quantitative Seismology*, Univ. Science Books, Mill Valley, Calif.

Besserer, J., F. Nimmo, M. A. Wieczorek, R. C. Weber, W. S. Kiefer, P. J. McGovern, J. C. Andrews-Hanna, D. E. Smith, and M. T. Zuber (2014), GRAIL gravity constraints on the vertical and lateral density structure of the lunar crust, *Geophys. Res. Lett.*, *41*(16), 5771–5777, doi:10.1002/2014GL060240.

Brzostowski, M., and A. Brzostowski (2009), Archiving the Apollo active seismic data, *The Leading Edge*, *28*(4), 414–416, doi:10.1190/1.3112756.

Cochard, A., H. Igel, B. Schuberth, W. Suryanto, A. Velikoseltsev, U. Schreiber, J. Wassermann, F. Scherbaum, and D. Vollmer (2006), Rotational motions in seismology: Theory, observation, simulation, in *Earthquake Source Asymmetry, Structural Media and Rotation Effects*, pp. 391–411, Springer., doi:10.1007/3-540-31337-0_30.

Cooper, M. R., R. L. Kovach, and J. S. Watkins (1974), Lunar near-surface structure, *Rev. Geophys.*, *12*(3), 291–308, doi:10.1029/RG012i003p00291.

Curtis, A., and J. O. A. Robertsson (2002), Volumetric wavefield recording and wave equation inversion for near-surface material properties, *Geophysics*, *67*(5), 1602–1611, doi:10.1190/1.1512751.

de Ridder, S. A. L., and B. L. Biondi (2015), Near-surface Scholte wave velocities at Ekofisk from short noise recordings by seismic noise gradiometry, *Geophys. Res. Lett.*, *42*(17), 7031–7038, doi:10.1002/2015GL065027.

Gangi, F. (1972), The lunar seismogram, *The Moon*, *4*, 40–48, doi:10.1007/BF00562913.

Goff, J. A., and K. Holliger (Eds.) (2003), *Heterogeneity in the Crust and Upper Mantle: Nature, Scaling, and Seismic Properties*, Kluwer Academic/Plenum Publishers, New York.

Horvath, P., G. V. Latham, Y. Nakamura, and H. J. Dorman (1980), Lunar near-surface shear wave velocities at the Apollo landing sites as inferred from spectral amplitude ratios, *J. Geophys. Res.*, *85*(B11), 6572–6578, doi:10.1029/JB085iB11p06572.

Khan, A., K. Mosegaard, and K. L. Rasmussen (2000), A new seismic velocity model for the Moon from a Monte Carlo inversion of the Apollo lunar seismic data, *Geophys. Res. Lett.*, *27*(11), 1591–1594, doi:10.1029/1999GL008452.

Korn, M. (1993), Seismic waves in random media, *J. Appl. Geophys.*, *29*(3), 247–269, doi:10.1016/0926-9851(93)90007-L.

Kovach, R., and J. Watkins (1973), The structure of the lunar crust at the Apollo 17 site, in *Proc. Lunar Sci. Conf. 4th*, pp. 2549–2560.

Langston, C. A. (2007a), Spatial gradient analysis for linear seismic arrays, *Bull. Seismol. Soc. Am.*, *97*(1B), 265–280, doi:10.1785/0120060100.

Langston, C. A. (2007b), Wave gradiometry in two dimensions, *Bull. Seismol. Soc. Am.*, *97*(2), 401–416, doi:10.1785/0120060138.

Langston, C. A. (2007c), Wave gradiometry in the time domain, *Bull. Seismol. Soc. Am.*, *97*(3), 926–933, doi:10.1785/0120060152.

Langston, C. A., P. Bodin, C. Powell, M. Withers, S. Horton, and W. Mooney (2006), Explosion source strong ground motions in the Mississippi embayment, *Bull. Seismol. Soc. Am.*, *96*(3), 1038–1054, doi:10.1785/0120050105.

Larose, E., A. Khan, Y. Nakamura, and M. Campillo (2005), Lunar subsurface investigated from correlation of seismic noise, *Geophys. Res. Lett.*, *32*(16), L16201, doi:10.1029/2005GL023518.

Latham, G. V., et al. (1970), Seismic data from man-made impacts on the Moon, *Science*, *170*(3958), 620–626, doi:10.1126/science.170.3958.620.

Liang, C., and C. A. Langston (2009), Wave gradiometry for USArray: Rayleigh waves, *J. Geophys. Res.*, *114*(B2), B02308, doi:10.1029/2008JB005918.

Lognonné, P., J. Gagnepain-Beyneix, and H. Chenet (2003), A new seismic model of the Moon: Implications for structure, thermal evolution and formation of the Moon, *Earth Planet. Sci. Lett.*, *211*(1–2), 27–44, doi:10.1016/S0012-821X(03)00172-9.

Muyzert, E., A. Kashubin, E. Kragh, and P. Edme (2012), Land seismic data acquisition using rotation sensors, *74th EAGE Conference & Exhibition EAGE, Extended Abstracts*, X033, doi:10.3997/2214-4609.20148780.

Nakamura, Y. (1983), Seismic velocity structure of the Lunar mantle, *J. Geophys. Res.*, *88*(B1), 677–686, doi:10.1029/JB088iB01p00677.

Nakamura, Y. (2011), Timing problem with the Lunar Module impact data as recorded by the LSPE and corrected near-surface structure at the Apollo 17 landing site, *J. Geophys. Res. E: Planets*, *116*(12), E12005, doi:10.1029/2011JE003972.

Poppeliers, C., and E. V. Evans (2015), The effects of measurement uncertainties in seismic-wave gradiometry, *Bull. Seismol. Soc. Am.*, *105*(6), 3143–3155, doi:10.1785/0120150043.

Robertsson, J. O. A., and A. Curtis (2002), Wavefield separation using densely deployed three-component single-sensor groups in land surface-seismic recordings, *Geophysics*, *67*(5), 1624–1633, doi:10.1190/1.1512809.

Schmelzbach, C., D. Sollberger, C. Van Renterghem, M. Häusler, J. Robertsson, and S. Greenhalgh (2016), Seismic spatial wavefield gradient and rotational rate measurements as new observables in land seismic exploration, *EGU General Assembly Conference Abstracts*, *18*, 3787.

Sollberger, D., C. Schmelzbach, C. Van Renterghem, J. O. A. Robertsson, and S. Greenhalgh (2016), Single-component elastic wavefield separation at the free surface using source- and receiver-side gradients, *SEG Technical Program Expanded Abstracts 2016*, 2268–2273, doi:10.1190/segam2016-13842637.1.

Telford, W. M., L. P. Geldart, and R. E. Sheriff (Eds.) (1990), *Applied Geophysics*, Cambridge Univ. Press, Cambridge, UK.

Spudich, P., L. K. Steck, M. Hellweg, J. B. Fletcher, and L. M. Baker (1995), Transient stresses at Parkfield, California, produced by the *M* 7.4 Landers earthquake of June 28, 1992: Observations from the UPSAR dense seismograph array, *J. Geophys. Res.*, *100*(B1), 675–690, doi:10.1029/94JB02477.

Stesky, R. M., and B. Renton (1977), Compressional and shear wave velocities in powdered rock under low loads, *Proc. Lunar Sci. Conf. 8th*, 1225–1233.

Talwani, P., A. Nur, and R. L. Kovach (1974), Implications of elastic wave velocities for Apollo 17 rock powders, *Proc. Lunar Sci. Conf. 5th*, 2919–2926.

Van Renterghem, C., C. Schmelzbach, and J. O. A. Robertsson (2016), Wavefield separation of multicomponent land seismic data using spatial wavefield gradients, *78th EAGE Conference & Exhibition, EAGE, Extended Abstracts*, doi:10.3997/2214-4609.201601357.

Virieux, J. (1986), P-SV wave propagation in heterogeneous media: Velocity-stress finite-difference method, *Geophysics*, *51*(4), 889–901, doi:10.1190/1.1442147.

Weber, R., P.-Y. Lin, E. J. Garnero, Q. Williams, and P. Lognonné (2011), Seismic detection of the lunar core, *Science*, *331*(6015), 309–312, doi:10.1126/science.1199375.

Wieczorek, M. A., et al. (2006), The constitution and structure of the lunar interior, *Rev. Mineral. Geochem.*, *60*(1), 221–364, doi:10.2138/rmg.2006.60.3.